fibers

MDPI

Communication

Electrochemical Oxidation of Pb II Using Carbon Electrodes Doped with Nanocellulose-FeOx

Araceli G. Gomez-Rojas [1], Luis Alejandro Macclesh del Pino-Perez [1,*], Carlos Fernando Castro-Guerrero [2], Claudia Esmeralda Ramos-Galvan [1] and Ana Beatriz Morales-Cepeda [1,*]

[1] Petrochemical Research Center, Technological Institute of Madero City—National Technological Institute of Mexico, Altamira 89600, Mexico
[2] CONACyT, Technological Institute of Madero City—National Technological Institute of Mexico, Altamira 89600, Mexico
* Correspondence: luis.mp@cdmadero.tecnm.mx (L.A.M.d.P.-P.); ana.mc@cdmadero.tecnm.mx (A.B.M.-C.)

Abstract: With TEMPO oxidation, it was possible to incorporate iron nanostructures into a cellulose nanofiber matrix. FTIR spectra showed the functional groups present in the films. The combination of both iron and CNF confers to the films good electrochemical activity; the electrochemical characterization (CV) showed that they present stability in the reduction process at a potential of 0–1 V, with the materials with 5% and 10% being the most active. The Pb reduction process shows that the 5% film is the material with the highest oxidizing capacity.

Keywords: nanocellulose; electrode; FeOx; PbII

Citation: Gomez-Rojas, A.G.; Macclesh del Pino-Perez, L.A.; Castro-Guerrero, C.F.; Ramos-Galvan, C.E.; Morales-Cepeda, A.B. Electrochemical Oxidation of Pb II Using Carbon Electrodes Doped with Nanocellulose-FeOx. *Fibers* **2023**, *11*, 8. https://doi.org/10.3390/fib11010008

Received: 3 November 2022
Revised: 4 January 2023
Accepted: 5 January 2023
Published: 12 January 2023

1. Introduction

At present, the synthesis of metallic nanostructures has gained great relevance due to its wide application in the fields of energy storage systems [1], biotechnology [2] and biomedicine [3–5], among others. Particularly, FeOx nanoparticles are of great interest due to their unique properties, such as their paramagnetic behavior and biocompatibility, as well as having the ability to have chemical arrangements on their surface [6]. Consequently, the range of applications of FeOx nanoparticles has grown in recent years. One of these applications is in the field of electrochemistry as an electrode coating material [7]. Heavy metals reaching water bodies, particularly lead as an industrial waste, pose a risk to public health and the environment due to its high toxicity and bioaccumulation [8–10]. It is widely accepted that the distribution and size of metal oxides in carbon-based matrices are crucial for improving the electrochemical performance of an electrode composed of metal oxides-carbon [11–13]. Cellulose-based matrices, as natural polymers, have gained importance as support for multiple materials. An example of these are cellulose nanofibers (CNFs) which are widely available from natural sources and often considered as waste [14–16], possessing properties such as flexibility, electrolyte absorption and a capability for developing films [17–20].

In accordance with the factors mentioned above, cellulose nanofibers are positioned as an ideal material for the dispersion of materials. On the other hand, it has been shown that negatively charged materials prepared based on nanocarbon and metal oxides have high electrochemical performance [21,22]. Lu et al. developed a new class of anode based on nanorods with Fe_2O_3, PEDOT Cores/Shells, demonstrating great electrochemical performance, high charge and flexibility [23].

The scope of this work is the use of electrodes composed of CNF-FeOx with added metal oxide concentrations of 1, 2.5, 5, 7.5 and 10 wt%, which were later implemented for the oxidation process of Pb(II) in an aqueous solution, observing the redox reaction of the heavy metal through cyclic voltammetry. Furthermore, the results of oxidizing the heavy metal showed films with good electrochemical stability during the oxidation process. The

synthesis process does not have any specific requirements for several conditions, such as temperature, pressure, additives or precursors, which simplifies the synthesis and negates the need for any high-cost materials. Due to the factors mentioned above, the films are an excellent option for treating polluted water with Pb.

2. Materials and Methods

For the preparation of the films, α-cellulose (particle size: 50 µm) and 2,2,6,6-tetramethylpiperidine-1-oxyl (TEMPO) were used; both of which were purchased from Sigma Aldrich (St. Louis, MO, USA). In addition, sodium bromide NaBr (99%), sodium hypochlorite NaOCl (6–9%), iron sulfate $FeSO_4$ (99%) and sodium hydroxide NaOH (99%) were purchased from Commercial brand Fermont. The solvent was triple distilled water.

For the synthesis of cellulose nanofibers, the method reported by Isogai et al. in 2007 [24], was implemented with modifications. For the TEMPO-mediated oxidation, α-cellulose was suspended in water and subjected to constant magnetic stirring at 400 rpm for a few minutes. Once the cellulose was homogenized in the liquid, 0.01 mmol TEMPO and 0.1 mmol NaBr were added. Iron sulfate was dissolved in 10 mL of water and added to the α-cellulose suspension. This mixture was later stirred for 5 min. Once the 5 min had passed, 13% sodium hypochlorite was added, starting the oxidation. The pH was monitored throughout the reaction to control it and keep it at a constant pH range of 10 by adding NaOH, dropwise. The entire process was carried out at room temperature.

After carrying out the TEMPO-mediated oxidation, the samples were washed through a centrifugation process at 2500 rpm for 10 min. This was repeated until any residue generated by the oxidation was eliminated and a neutral pH was obtained. Once the washing was finished, the suspension was dialyzed to remove low molecular weight ions and impurities. Once the solutions were ready, the films were prepared by casting using 6 mL of the solution for each film, which was poured into a 4 cm. diameter mold. The films were dried at 30 °C for 3 days until complete evaporation of the solvent. Once the films were formed, they were removed from the mold for further analyses (Figure 1). The films were analyzed through Fourier Transform Infrared Spectroscopy, using a Perkin Elmer Spectrum 100 Spectrophotometer (form Waltham, MA, USA) for the functional group's identifications. The CNF-Fe and CNC were analyzed using a range of 4000 and 500 cm^{-1}, with a resolution of 5 cm^{-1} and 16 scans.

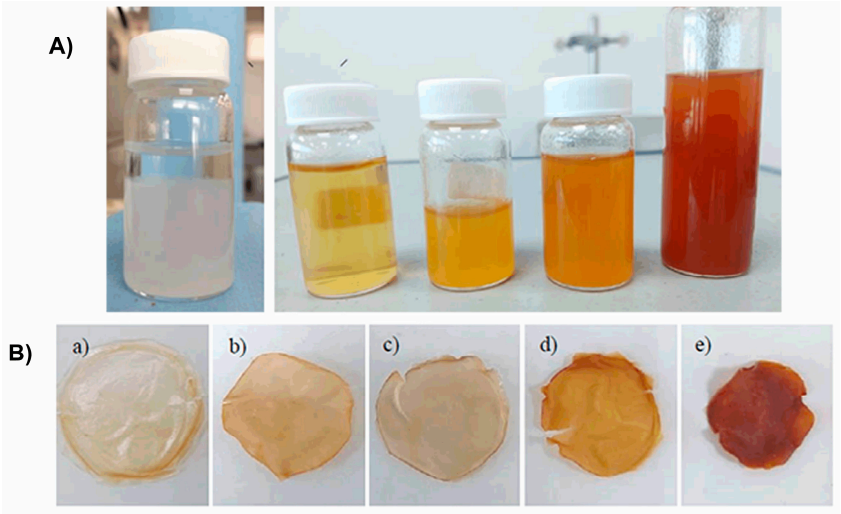

Figure 1. (**A**) Nanocellulose solutions at different concentrations. (**B**) CNF-Fe films with (**a**) 1% *w*/*w* Fe, (**b**) 2.5% *w*/*w* Fe, (**c**) 5% *w*/*w* Fe, (**d**) 7.5% *w*/*w* Fe, (**e**) 10% *w*/*w* Fe.

Particle size distribution was determined in solution 0.1 mg/mL by dynamic light scattering using a Malvern Instrument Zetazizer Nano ZS model manufacturer ir Malvern Instrument from Malvern, UK,

The electrochemical stability and oxidative capacity of Pb solutions (5 µM of Pb in a 4.4 pH buffer) were carried out by cyclic voltammetry in a Metrohm potentiostat 910 PSTAT mini.

3. Results

In Figure 2, we can observe the FTIR spectrum of the nanocellulose films with added iron oxide. In the spectrum corresponding to the oxidized TEMPO nanofibers, a peak at 3336 cm^{-1} is visible, representative of the stretching of the hydrogen bonding of the -OH groups present in the cellulosic compound, as well as stretching of the -CH groups in the band with a 2905 cm^{-1} wavelength [25]. A peak is observed at 1597 cm^{-1}, corresponding to the C=O stretching (at 1700 cm^{-1}), which are displaced due to oxidation during treatment; this change is due to the hydroxyl groups of "C6" being changed by sodium carboxyl ions [26,27]. The peak at 1407 cm^{-1} corresponds to the CH vibrations of cellulose and, due to -OH vibrations, a peak can be seen at a wavelength of 1371 cm^{-1}. The transmittance in the regions of 1500 cm^{-1} and 1000 cm^{-1} imply pyranose ring bending and vibrations of the nanocellulose backbone [28]. The signal at 1202 cm^{-1} represents C-O-C stretching of the ether groups [29].

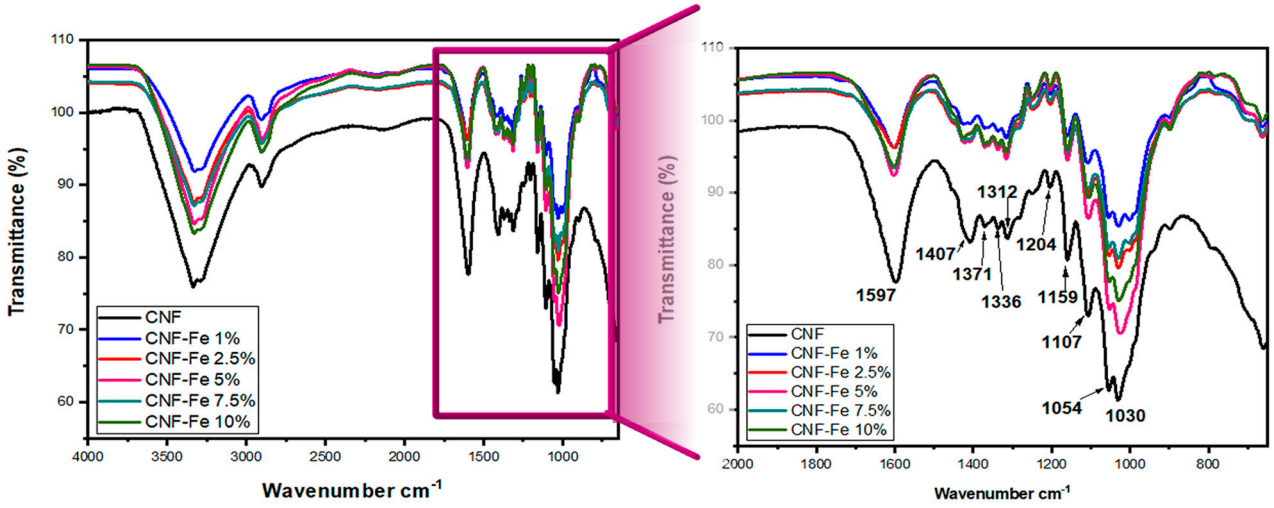

Figure 2. FTIR spectrum of CNF and CNF-iron oxide films.

In addition, a peak corresponding to the asymmetric stretching of C-O is observed at 1159 cm^{-1}, while the peaks at 1054 and 1030 cm^{-1} represent the skeletal vibration of the C-O-C pyranose ring [30]. The spectra of nanocellulose with iron exhibits a significant change in peak intensities but maintain similar positions. These changes are due to the incorporation of oxidized iron particles, since these displace sodium from the fiber [27], in Table 1 is shown the functional groups.

Table 1. Functional groups.

Wavenumber (cm^{-1})	Assignation	Reference
3336	O-H Stretching vibration	Zhang X. et al. [25]
2905	CH-Stretching vibration	Zhang X. et al. [25]
1579	C=O Streching vibration	Castro-Guerrero et al. [26]
1407	CH_2- Pyranose ring Vibration	Pastorova, I. [28]
1202	C-O-C Streching	Rai, K. [29]

The dynamic light scattering (DLS) technique is a very useful tool for particle size determination. This technique is widely used to determine the size of particles with a certain sphericity in colloidal suspensions [31]. However, in the case of structures such as rods or fibers, this technique presents limitations in particle size precision, since the

obtained range depends on the orientation of the fibers in the fluid; therefore, the value of the particle size will only be an approximate value [32]. As this technique assumes that any particle has a crystalline sphericity of equivalent volume, the radius corresponds to the hypothetical radius of a solid sphere with the same diffusion coefficient as the particles being investigated [33].

Figure 3top shows the particle size distribution of CNF. We can observe two signals that represent the fiber diameter, with an average close to 100 nm. These signals are similar to those reported by Chandravati et al. [34], while interpreting the last signal as the length of the fiber, close to 800 nm.

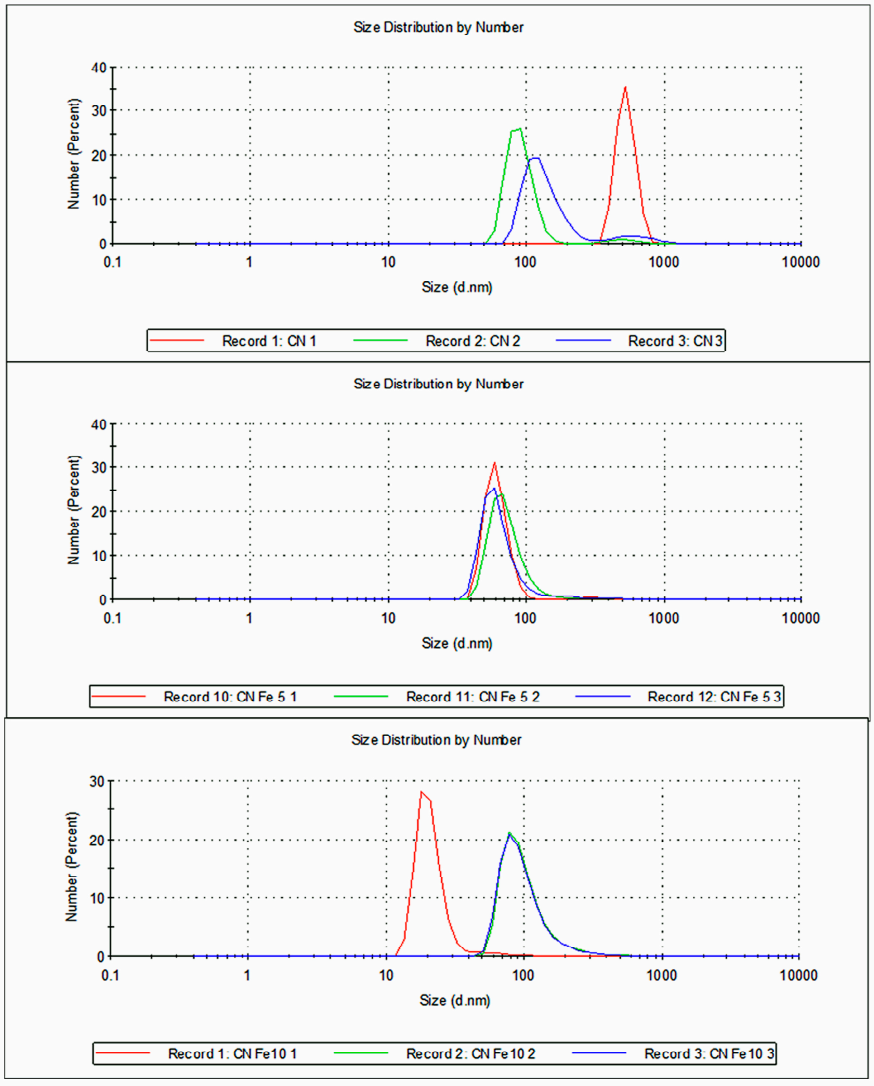

Figure 3. Size distribution of (**top**) CNF; (**middle**) CN-Fe 5%; and (**bottom**) CNF-Fe 10%.

Figure 3middle shows the particle size distribution of the 5 wt% CNF-FeOx material, in which, a particle size distribution close to 70 nm is presented. In Figure 3bottom, the signals of the 10 wt% CNF-FeOx material are shown. Despite the different concentrations of iron, all of them present a similar particle size, around 100 nm, which we can relate to the length of the particle. In addition, the analysis shows a repeatability in the calculation of the particle size in each graph, confirming the measurements. This places them within the nanocrystals size range, which have reported diameters between 2 and 20 nm and lengths between 100 and 600 nm [35].

Figure 4 shows the cyclic voltammogram for the carbon electrode, the carbon electrode modified with CNF-Fe (C/CNF-Fe) at 1%, 2.5%, 5%, 7.5% and 10% iron, using a pH of

4.2 with buffer solution. The materials exhibited stability on the redox process at a 0–1 V potential. Among the MOx that have been studied, many present an oxidation or reduction tendency under certain conditions, particularly FeOx species coupled with organic species, which tend to have an improvement in their electrochemical properties [36–38].

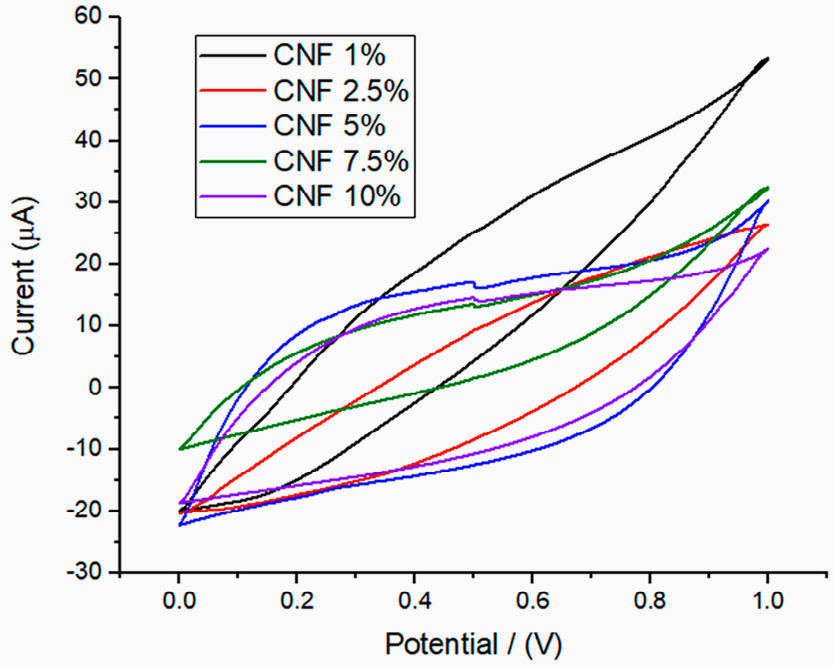

Figure 4. Cyclic voltammogram of a carbon electrode and carbon electrodes modified with CNF-Fe (C/CNF-Fe) at different iron percentages 1%, 2.5%, 5%, 7.5% and 10%, using a pH 4.2 buffer solution.

Well-defined anodic and cathodic peaks are observed in Figure 4, with the oxidation and reduction potential varying by approximately 0.1 V. The voltammogram shows that the material with 1% Fe presents a moderate electrochemical activity with a slight tendency to reduction, as well as the materials with 2.5% and 7.5%, all presenting electrochemical stability in the process [39]. On the other hand, materials with 5% and 10% Fe present a higher amplitude in the current due to a higher electrochemical activity [40]. Overall, materials do not change after the CV, indicating excellent structural integrity [41].

Figure 5 shows the voltammetry curves for the carbon electrode and the carbon electrodes modified with CNF-FeOx, employing a 4.2 pH buffer solution with 100 μg/L of Pb. The CV shows that all the reactions prove to be reversible and have an increase in the current response for the electrodes modified with CNF-FeOx compared to the carbon electrode, with the C/CNF-Fe 1%- and C/CNF-Fe 5%-modified electrodes presenting a greater range of current in their response, in addition to having a well-defined anodic peak.

$$Pb^{2+}(aq) + 2e^{-} \rightarrow Pb(s) \text{ Reduction reaction}$$

$$Pb(s) \rightarrow Pb^{2+}(aq) + 2e^{-} \text{ Oxidation reaction}$$

Greater current generation suggests that CNF-Fe facilitated electron transfer from the electrolyte to the electrode and there was a higher diffusion of Pb on the electrode surface [42]. Therefore, the electron transfer kinetics are improved in the electrode with C/CNF-FeOx 5%.

For the material with 1% Fe, the Pb reduction process starts close to −0.8 V, and reversibility of the oxidation process starts at −0.45 V; naturally, the oxidation process is more evident [43]. The reaction that develops is as follows:

$$Pb^{2+}(aq) + 2e^{-} \rightarrow Pb(s) \text{ Reduction reaction}$$

$$Pb(s) \rightarrow Pb^{2+}(aq) + 2e^{-} \text{ Oxidation reaction}$$

The C/CNF-Fe 5% electrode exhibits a similar behavior to the C/CNF-Fe 1% electrode, presenting a reduction process close to −0.82 V, this process being much lower than the 1% electrode. However, the oxidation process occurs at −0.38 V, and in this case, the oxidation process is higher than with the 1% film. This curve has a marked tendency to Pb oxidation [44]. The rest of the electrodes present similar behaviors based on the reversibility process and, like the first two, they also present a notable tendency to the oxidation reaction.

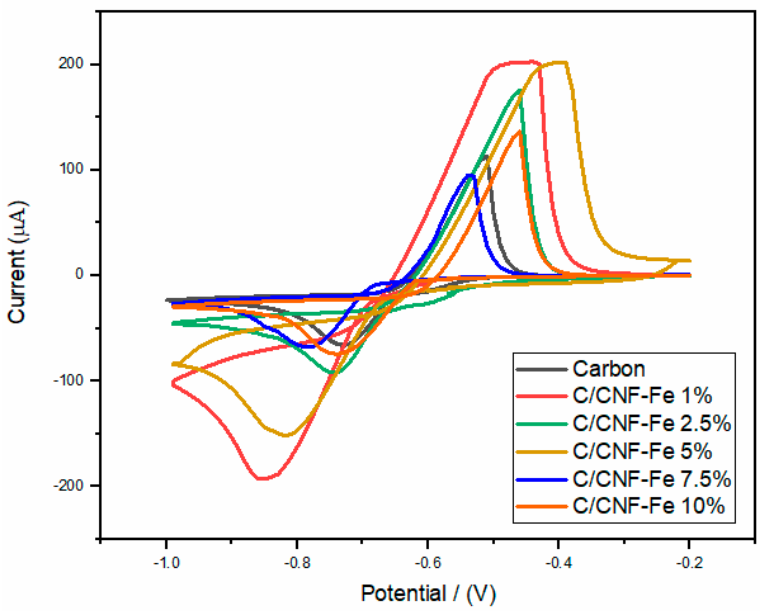

Figure 5. Cyclic voltamogram of a carbon electrode and carbon electrodes modified with CNF-Fe (C/CNF-Fe) at different iron percentages 1%, 2.5%, 5%, 7.5% and 10%, employing a 4.2 pH buffer solution with 100 μg/L of Pb.

Comparing responses of the carbon electrode and the electrodes with CNF-FeOx, it is possible to appreciate a notable difference in the current intensities of the signals, this is possibly due to the cellulose nanofibers providing a network which facilitates needed routes for electron transfer and better electrochemical behavior, boosting the ion transfer process on the electrode surface (Figure 6).

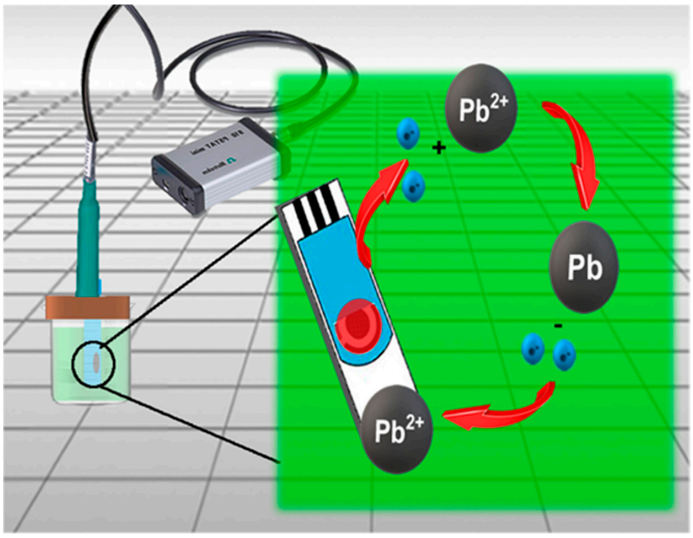

Figure 6. Representation of CNF-FeOx electrode in Pb redox process.

Table 2 shows modified electrodes previously reported in the literature, which were employed to quantify heavy metals in water by means of electrochemistry. As shown in the table, the detection limit obtained from the C/CNF-Fe 5% electrode is like some of the previously tested materials, showing that the C/CNF-Fe5 % electrode can be used not only for Pb(II) oxidation but also for its detection, since it exhibits a good detection capacity.

Table 2. Comparison of modified electrodes for the determination of Pb.

Electrode Material	Ion	Concentration (μM)	LOD (μM)	Ref.
Boron-doped nanocrystalline diamond (BD-NCD)	Pb(II)	1–22.5	1.399	[45]
Amino-Carbon microsphere (NH2-CMS)	Pb(II)	0.5–1.2	0.05	[46]
Copper mini-sensor modified with bismuth	Pb(II) Cd(II)	1.3–13	0.8	[47]
Antimony Nanoparticle Modified Boron-Doped Diamond Electrode	Pb(II) Cd(II)	0.2–2.41	0.12	[48]
Terephthalic acid capped iron oxide nanoparticles	Pb(II) Cd(II) Hg(II)	0.4–1.1	0.04	[42]
Crown Ether-modified Electrodes	Pb(II) Cd(II) Hg(II)	0.2–0.9	0.05	[49]
Carbon electrode modified with CNF-Fe 5 %	Pb(II)	0.2–1.2	0.23	Present work

4. Conclusions

The results show that the methodology implemented by Isogai et al., later modified by Macclesh et al. [24,27], is a viable alternative to incorporate metal particles into cellulose nanofibers. Particularly, our prepared materials proved to have the needed characteristics to be implemented as electrodes, either as an electrode for detecting the presence of Pb(II) in an aqueous system or, in a more specific aspect, they present the capability to oxidize lead ions. The latter being fundamental for treatment of water effluents resulting from industrial processes (i.e., mining, oil, agriculture), mitigating the environmental impact of these economic sectors.

Author Contributions: Methodology, L.A.M.d.P.-P. and A.B.M.-C.; Investigation, A.G.G.-R.; Writing—original draft, L.A.M.d.P.-P.; Writing—review C.F.C.-G.; Supervision, C.E.R.-G.; Project administration, A.B.M.-C. All authors have read and agreed to the published version of the manuscript.

Funding: The authors would like to express their gratitude to Tecnológico Nacional de México for their project number TNM 15035.22-P "ELECTRODO DE NANOCELULOSA-FEO3 PARA LA OXIDACION DE TRAZAS DE Pb EN SOLUCION ACUOSA" support with this work. Gomez Rojas would like to express her gratitude to Conacyt for the scholarship 1086146. This project was carried out in the postgraduate course in Master of Science in Chemical Engineering (MCIQ).

Data Availability Statement: Not applicable.

Conflicts of Interest: The authors declare no conflict of interest.

References

1. Kang, Y.S.; Risbud SRabolt, J.F.; Stroeve, P. Synthesis and characterization of nanometer-size Fe_3O_5 and γ-Fe_2O_3 particles. *Chem. Mater.* **1996**, *8*, 2209–2211. [CrossRef]
2. Pankhurst, Q.A.; Connolly, J.; Jones, S.K.; Dobson, J. Applications of magnetic nanoparticles in biomedicine. *J. Phys. D Appl. Phys.* **2003**, *36*, R167. [CrossRef]
3. Dobson, J. Gene therapy progress and prospects: Magnetic nanoparticle-based gene delivery. *Gene Ther.* **2006**, *13*, 283–287. [CrossRef]

4. Rudgne, S.; Peterson, C.; Vessely, C.; Koda, J.; Stevens, S.; Catterall, L. Adsorption and desorption of chemotherapeutic drugs from a magnetically carrier (MTC). *J. Control. Release* **2001**, *74*, 335–340. [CrossRef] [PubMed]
5. Appenzeller, T. The Man Who Dared to Think Small. *Science* **1991**, *254*, 1300. [CrossRef] [PubMed]
6. Issa, B.; Obaidat, I.M.; Albiss, B.A.; Haik, Y. Magnetic nanoparticles: Surface effects and properties related to biomedicine appli-cation. *Int. J. Mol Sci.* **2013**, *14*, 21266–21305. [CrossRef] [PubMed]
7. Sun, R.; Gao, J.; Wu, G.; Liu, P.; Guo, W.; Zhou, H.; Ge, J.; Hu, Y.; Xue, Z.; Li, H.; et al. Amorphous Metal Oxide Nanosheets Featuring Reversible Structure Transformations as Sodium-Ion Battery Anodes. *Cell Rep. Phys. Sci.* **2020**, *1*, 100118. [CrossRef]
8. Hua, M.; Zhang, S.; Pan, B.; Zhang, W.; Lv, L.; Zhang, Q. Heavy metal removal from water/wastewater by nanosized metal oxides: A review. *J. Hazard. Mater.* **2012**, *211*, 317–331. [CrossRef] [PubMed]
9. Davis, T.A.; Volesky, B.; Mucci, A. A review of the biochemistry of heavy matel biosorption by brown algae. *Water Res.* **2003**, *37*, 43311–44330. [CrossRef] [PubMed]
10. Chai, L.; Wang, Q.; Li, Q.; Yang, Z.; Wang, Y. Enhanced removal of Hg(II) from acidic aqueous solution using thiol-functionalized biomass. *Water Sci. Technol.* **2010**, *62*, 2157–2166. [CrossRef] [PubMed]
11. Peng, C.; Chen, B.; Qin, Y.; Yang, S.; Li, C.; Zuo, Y.; Liu, S.; Yang, J. Facile Ultrasonic Synthesis of CoO Quantum Dot/Graphene Nanosheet Composites with High Lithium Storage Capacity. *ACS Nano* **2012**, *6*, 1074–1081. [CrossRef] [PubMed]
12. Sun, X.; Zhou, C.; Xie, M.; Sun, H.; Hu, T.; Lu, F.; Scott, S.M.; George, S.M.; Lian, J. Synthesis of ZnO quantum dot/graphene nanocomposites by atomic layer deposition with high lithium storage capacity. *J. Mater. Chem. A* **2014**, *2*, 7319–7326. [CrossRef]
13. Wu, Z.-S.; Zhou, G.; Yin, L.-C.; Ren, W.; Li, F.; Cheng, H.-M. Graphene/metal oxide composite electrode materials for energy storage. *Nano Energy* **2012**, *1*, 107–131. [CrossRef]
14. Kongruang, S. Bacterial cellulose production by Acetobacter xylinum strains from agricultural waste products. In *Biotechnology for Fuels and Chemicals, Proceedings of the ABAB Symposium (Part A: Enzyme Engineering and Biotechnology), Denver, CO, USA, 29 April–2 May 2007*; Adney, W.S., McMilland, J.D., Mielenz, J., Klasson, K.T., Eds.; Humana Press: Totowa, NJ, USA, 2007. [CrossRef]
15. Basavaraj, S.H.; Gupta, S.G. Production of bacterial cellulose from Enterobacter amnigenus GH-1 isolated from rotten apple. *World J. Microbiol. Biotechnol.* **2010**, *26*, 1823–1828.
16. Fernando, C.G.C.; Thomas, H.; Andreas, K.; Beatriz, M.C.A.; Uzziel, P.B.E.; María, Z.A. Isolation of Cellulose Nanocrystals from Thypha domingensis Named Southern Cattail Using a Batch Reactor. *Fibers Polym.* **2019**, *20*, 1136–1144.
17. Gui, Z.; Zhu, H.; Gillette, E.; Han, X.; Rubloff, G.W.; Hu, L.; Lee, S.B. Natural Cellulose Fiber as Substrate for Supercapacitor. *ACS Nano* **2013**, *7*, 6037–6046. [CrossRef] [PubMed]
18. Wang, Z.; Tammela, P.; Strømme, M.; Nyholm, L. Cellulose-based Supercapacitors: Material and Performance Considerations. *Adv. Energy Mater.* **2017**, *7*, 1700130. [CrossRef]
19. Weng, Z.; Su, Y.; Wang, D.-W.; Li, F.; Du, J.; Cheng, H.-M. Graphene-Cellulose Paper Flexible Supercapacitors. *Adv. Energy Mater.* **2011**, *1*, 917–922. [CrossRef]
20. Gao, K.; Shao, Z.; Li, J.; Wang, W.; Peng, X.; Wang, W.; Wang, F. Cellulose nanofiber-graphene all solid-state flexible supercapacitors. *J. Mater. Chem. A* **2013**, *1*, 63–67. [CrossRef]
21. Li, Y.; Xu, J.; Feng, T.; Yao, Q.; Xie, J.; Xia, H. Fe_2O_3Nanoneedles on Ultrafine Nickel Nanotube Arrays as Efficient Anode for High-Performance Asymmetric Supercapacitors. *Adv. Funct. Mater.* **2017**, *27*, 1606728. [CrossRef]
22. Sun, J.; Huang, Y.; Fu, C.; Huang, Y.; Zhu, M.; Tao, X.; Zhi, C.; Hu, H. A high-performance fiber-shaped PEDOT@MnO_2//C@Fe_3O_4 asymmetric supercapacitor for wearable electronics. *J. Mater. Chem. A* **2016**, *4*, 14877–14883. [CrossRef]
23. Lu, X.; Zeng, Y.; Han, Y.; Zhao, Y.; Zeng, Y.; Yu, M.; Liu, Y.; Tang, H.; Ton, Y. Advanced Ti-Doped Fe2O3@PEDOT Core/Shell Anode for High-Energy Asymmetric Supercapacitors. *Adv. Energy Mater.* **2015**, *5*, 1402176.
24. Saito, T.; Kimura, S.; Nishiyama, Y.; Isogai, A. Cellulose Nanofibers Prepared by TEMPO-Mediated Oxidation of Native Cellulose. *Biomacromolecules* **2007**, *8*, 2485–2491. [CrossRef] [PubMed]
25. Zhang, X.; Sun, H.; Tan, S.; Gao, J.; Fu, Y.; Liu, Z. Hydrothermal synthesis of Ag nanoparticles on the nanocellulose and their antibacterial study. *Inorg. Chem. Commun.* **2019**, *100*, 44–50. [CrossRef]
26. Castro-Guerrero, C.F.; Gray, D.G. Chiral nematic phase formation by aqueous suspensions of cellulose nanocrystals prepared by oxidation with ammonium persulfate. *Cellulose* **2014**, *21*, 2567–2577. [CrossRef]
27. Macclesh del Pino, L.A.; Morales, A.B.; Castro, C.F.; Leon, U. In situ synthesis of Ag/AgCl nanoparticles in a Cellulose nanofibers matrix via in situ: A conductive paper. *Cellulose* **2021**, *10*, 1–13.
28. Pastorova, I.; Botto, R.E.; Arisz, P.W.; Boon, J.J. Cellulose char structure: A combine analytical Py-GC-MS, FTIR and NMR study. *Carbohydr. Res.* **1994**, *262*, 27–47. [CrossRef]
29. Rai, K.S. Methylcellulose synthesis from corn cobs study of the effect of solvent 421 conditions on product properties by thermal analysis. *J. Therm. Anal. Calorim.* **2013**, *114*, 809.
30. Park, M.; Cheng, J.; Choi, J.; Kim, J.; Hyun, J. Elecromagnetic nanocomposite of bacterial cellulose using magnetite nanoclusters and polyaniline. *Colloids Surf. B Biointerfaces* **2013**, *102*, 238–242. [CrossRef]
31. Chu, B.; Liu, T. Characterization of nanoparticles by scattering techniques. *J. Nanoparticles Res.* **2000**, *2*, 29–41. [CrossRef]
32. Frone, A.N.; Panaitescu, D.M.; Spataru, D.D.; Radovici, C.; Trusca, R.; Somoghi, R. Preparation and characterization of PVA composites with cellulose nanofibers obtained by ultrasonication. *BioResources* **2011**, *6*, 487–512. [CrossRef]
33. Fraschini, C.; Chauve, G.; Le Berre, J.-F.; Methot, M.; O'Connor, B.; Bouchard, J. Critical discussion of light scattering and mi-croscopy techniques for CNC particle sizing. *Nord. Pulp Pap. Res. J.* **2014**, *29*, 31–40. [CrossRef]

34. Yadav, C.; Saini, A.; Maji, P.K. Energy efficient facile extraction process of cellulose nanofibers and their dimensional characterization using their dimensional characterization using light. *Carbohydr. Polym.* **2017**, *165*, 276–284. [CrossRef] [PubMed]
35. Aucrsch, A.; Littke, W.; Lang, P.; Burchard, W. Static and dynamic light scattering on solutions of precrystalline be-ta-galactosidase. *J. Cryst. Growth* **1991**, *110*, 201–207. [CrossRef]
36. Jin, B.; Liu, A.-H.; Liu, G.-Y.; Yang, Z.-Z.; Zhong, X.-B.; Ma, X.-Z.; Yang, M.; Wang, H.-Y. Fe_3O_4–pyrolytic graphite oxide composite as an anode material for lithium secondary batteries. *Electrochim. Acta* **2013**, *90*, 426–432. [CrossRef]
37. Lv, H.; Jiang, R.; Li, Y.; Zhang, X.; Wang, J. Microemulsion-mediated hydrothermal growth of pagoda-like Fe3O4 microstructures and their application in a lithium–air battery. *Ceram. Int.* **2015**, *41*, 8843–8848. [CrossRef]
38. Lei, Y.; Lu, J.; Luo, X.; Wu, T.; Du, P.; Zhang, X.; Ren, Y.; Wen, J.; Miller, D.J.; Miller, J.T.; et al. Synthesis of Porous Carbon Supported Palladium Nanoparticle Catalysts by Atomic Layer Deposition: Application for Rechargeable Lithium–O_2 Battery. *Nano Lett.* **2013**, *13*, 4182–4189. [CrossRef]
39. Lee, K.K.; Deng, S.; Fan, H.M.; Mhaisalkar, S.; Tan, H.R.; Tok, E.S.; Loh, K.P.; Chin, W.S.; Sow, C.H. α-Fe_2O_3 nanotubes-reduced graphene oxide composites as synergistic electrochemical capacitor materials. *Nanoscale* **2012**, *4*, 2958–2961. [CrossRef]
40. Brown, I.J.; Sotiropoulos, S. Electrodeposition of Ni from a high internal phase emulsion (HIPE) template. *Electrochim. Acta* **2001**, *46*, 2711–2720. [CrossRef]
41. Xia, L.; Li, X.; Wu, X.; Huang, L.; Liao, Y.; Qing, Y.; Wu, Y.; Lu, X. Fe_3O_4 nanoparticles embedded in cellulose nanofibre/graphite carbon hybrid aerogels as advanced negative electrodes for flexible asymmetric supercapacitors. *J. Mater. Chem. A* **2018**, *6*, 17378–17388. [CrossRef]
42. Deshmukh, S.; Kandasamy, G.; Upadhyay, R.K.; Bhattacharya, G.; Banerjee, D.; Maity, D.; Deshusses, M.A.; Roy, S.S. Terephthalic acid capped iron oxide nanoparticles for sensitive electrochemical detection of heavy metal ions in water. *J. Electroanal. Chem.* **2017**, *788*, 91–98. [CrossRef]
43. Ganesh, V.; Lakshminarayanan, V. Preparation of high surface area nickel electrodeposit using a liquid crystal template technique. *Electrochim. Acta* **2004**, *49*, 3561–3572. [CrossRef]
44. Nan, H.; Yu, L.; Ma, W.; Geng, B.; Zhang, X. Flexible superior electrode architectures based on three-dimensional porous spinous α-Fe_2O_3 with a high performance as a supercapacitor. *Dalton Trans.* **2015**, *44*, 9581–9587. [CrossRef]
45. Nurhayati, E.; Juang, Y.; Rajkumar, M.; Huang, C.; Hu, C.-C. Effects of dynamic polarization on boron-doped NCD properties and on its performance for electrochemical-analysis of Pb (II), Cu (II) and Hg (II) in aqueous solution via direct LSV. *Sep. Purif. Technol.* **2015**, *156*, 1047–1056. [CrossRef]
46. Sun, Y.-F.; Zhao, L.-J.; Jiang, T.-J.; Li, S.-S.; Yang, M.; Huang, X.-J. Sensitive and selective electrochemical detection of heavy metal ions using amino-functionalized carbon microspheres. *J. Electroanal. Chem.* **2016**, *760*, 143–150. [CrossRef]
47. Figueiredo-Filho, L.C.S.; Janegitz, B.C.; Fatibelilo-Filho, O.; Marcolino-Junior, L.H.; Banks, C.E. Inexpensive and disposable copper mini-sensor modified with bismuth for lead and cadmium determination using square-wave anodic stripping voltammetry. *Anal. Methods* **2013**, *5*, 202–207. [CrossRef]
48. Toghill, K.E.; Xiao, L.; Wildgoose, G.G.; Compton, R.G. Electroanalytical Determination of Cadmium(II) and Lead(II) Using an Antimony Nanoparticle Modified Boron-Doped Diamond Electrode. *Electroanalysis* **2009**, *21*, 1113–1118. [CrossRef]
49. González-Calabuig, A.; Guerrero, D.; Serrano, N.; del Valle, M. Simultaneous Voltammetric Determination of Heavy Metals by Use of Crown Ether-modified Electrodes and Chemometrics. *Electroanalysis* **2016**, *28*, 663–670. [CrossRef]